ACS NANO

www.acsnano.org

ARTICLE

Materials Combining Asymmetric Pore Structures with Well-Defined Mesoporosity for Energy Storage and Conversion

Sarah A. Hesse,[¶] Kevin E. Fritz,[¶] Peter A. Beaucage, R. Paxton Thedford, Fei Yu, Francis J. DiSalvo, Jin Suntivich, and Ulrich Wiesner*

Cite This: https://dx.doi.org/10.1021/acsnano.0c05903

Read Online

ACCESS | Metrics & More | Article Recommendations | Supporting Information

ABSTRACT: Porous materials design often faces a trade-off between the requirements of high internal surface area and high reagent flux. Inorganic materials with asymmetric/hierarchical pore structures or well-defined mesopores have been tested to overcome this trade-off, but success has remained limited when the strategies are employed individually. Here, the attributes of both strategies are combined and a scalable path to porous titanium nitride (TiN) and carbon membranes that are conducting (TiN, carbon) or superconducting (TiN) is demonstrated. These materials exhibit a combination of asymmetric, hierarchical pore structures and well-defined mesoporosity throughout the material. Fast transport through such TiN materials as an electrochemical double-layer capacitor provides a substantial improvement in capacity retention at high scan rates, resulting in state-of-the-art power density (28.2 kW kg^{-1}) at competitive energy density (7.3 W-h kg^{-1}). In the case of carbon membranes, a record-setting power density (287.9 kW kg^{-1}) at 14.5 W-h kg^{-1} is reported. Results suggest distinct advantages of such pore architectures for energy storage and conversion applications and provide an advanced avenue for addressing the trade-off between high-surface-area and high-flux requirements.

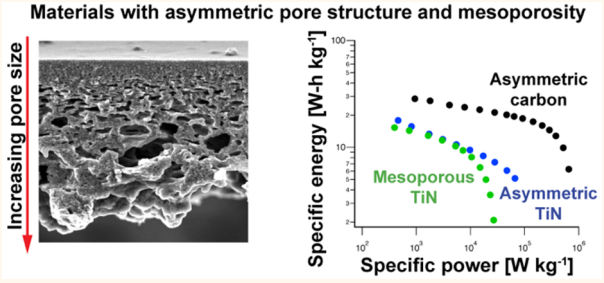

KEYWORDS: *block copolymers, self-assembly, mesoporous materials, asymmetric porosity, capacitors*

The ability to prepare mesoporous materials with interconnected pores has resulted in improvements in power[1,2] and energy densities in energy storage devices.[3,4] However, at fast charge/discharge rates, only a small fraction of pores are accessible, resulting in pore underutilization. While pore utilization can be improved by reducing the electrode thickness,[5] there is a trade-off between energy density and rate capability (*i.e.*, power density). This Goldilocks issue has restricted energy storage devices such as batteries and capacitors from achieving both high energy and power densities.[6−8] Even for electrochemical double-layer capacitors (EDLCs), a device known for high power density, the energy density drops precipitously at high rate operation. For example, mesoporous carbon with the presence of microporosity to substantially increase the surface area has been used to make EDLCs with high energy density (>10 W-h kg^{-1}).[3] However, these energy densities can only be realized at moderate power densities (<10^2 kW kg^{-1}).[3] To improve the rate capability, hierarchical carbon structures, consisting of a combination of macro-, meso-, and microporosity, have been explored. While these structures allow improved power density,[9] realizing simultaneously improved energy and power densities has not been straightforward even when these hierarchical structures have high specific surface areas comparable to energy-dense mesoporous structures. Other strategies such as making the pores ionophobic to enhance charge storage,[10,11] modifying the pore shape to reduce internal resistance,[12] and modeling ion transport during charging and discharging[13] have also been studied; however, the issue of pore underutilization remains. This observation points to a critical need for a strategy to overcome pore underutilization in hierarchical structures to enable high energy densities at high rate operation.

Nature employs asymmetric structures to address this trade-off between requirements for high internal surface area and high flux. For example, the respiratory system is highly

Received: July 15, 2020
Accepted: November 16, 2020

asymmetric in structure and uses airflow through the trachea and bronchi to the alveoli in order to allow high flux while simultaneously providing a large surface area for O_2/CO_2 exchange. Creating engineered asymmetric inorganic structures with graded porosity requires nonequilibrium processes, however, which has remained challenging. One approach has employed non-solvent-induced phase separation (NIPS) to prepare asymmetric carbon structures, a widely used and scalable industrial ultrafiltration polymer membrane formation process.[14] These structures possess an asymmetric, hierarchical structural gradient consisting of macro- to micropores, the latter of which particularly aid in obtaining high surface areas.[15−17] However, because these structures lack well-defined mesopores throughout the membrane, they face the same pore inaccessibility restriction: their high energy density (>10 W-h kg^{-1}) can only be realized at modest power density (<10 kW kg^{-1}).[15,17]

To address these shortcomings and produce EDLCs with high energy density (>10 W-h kg^{-1}) at a high power density (>250 kW kg^{-1}), here we combine structural asymmetry, including hierarchical porosity, with well-defined mesoporosity throughout the material. Our approach integrates three processes: inorganic materials formation, NIPS, and block copolymer (BCP) self-assembly (SA). Our approach is different from the NIPS process, which has traditionally been exclusively used with homopolymers.[14] While the NIPS process produces asymmetric structures with graded, *i.e.*, hierarchical, porosity, the resulting membranes lack well-defined mesopores throughout the material. Furthermore, while NIPS membranes from homopolymers such as polyacrylonitrile (PAN) can be converted into asymmetric carbon structures through thermal processing,[15,17] it is not straightforward to use this process to produce asymmetric membranes from other inorganic materials. Our combination of BCP SA and NIPS (SA + NIPS = SNIPS) circumvents all these issues. It has already provided a paradigm shift in the ability to generate high flux and high resolution asymmetric organic polymer ultrafiltration (UF) membranes.[18,19] Here we translate this success from soft nanostructures to the direct formation of asymmetric porous carbon structures and asymmetric inorganic porous nitrides. Rather than using asymmetric polymer membranes as templates, requiring laborious backfilling steps that are not easily scalable, polymer and inorganic precursors mixed in a dope solution are submitted to the SNIPS process together. Subsequent thermal processing leads to final inorganic membranes combining structural pore asymmetry with homogeneous mesopores throughout the macropore walls. In the case of carbon, the resulting membranes further exhibit micropores that contribute additionally to the structures' internal surface areas.

Crucially, we demonstrate that such membranes substantially enhance mass transport of ions in EDLCs and allow for high rate capability without compromising on available surface area, outperforming previous materials with pore architectures including purely asymmetric, mesoporous, or hierarchical structures. We attribute these improvements to the combination of structural asymmetry, which allows rapid ion transport, with well-defined mesoporosity throughout, consequently aiding pore accessibility. Efforts will start with titanium nitride (TiN), a promising alternative material for aqueous EDLCs, owing to its high conductivity, corrosion resistance, and wide voltage window.[20] In order to gain fundamental insights into the effects of the asymmetric structure on transport, we compare asymmetric TiN with well-defined mesopores (for simplicity in the following referred to as "asymmetric TiN") to a periodically ordered, mesoporous TiN monolith derived from BCP SA and mimicking conventional mesoporous materials used in EDLC applications. We also synthesize asymmetric graphitic carbon and measure its capacitive performance to demonstrate that the combination of structural asymmetry and well-defined mesopores can be extended to enhance micropore accessibility.

RESULTS AND DISCUSSION

Asymmetric Inorganic Material Synthesis and Characterization. Figure 1 shows the overall synthesis flow.

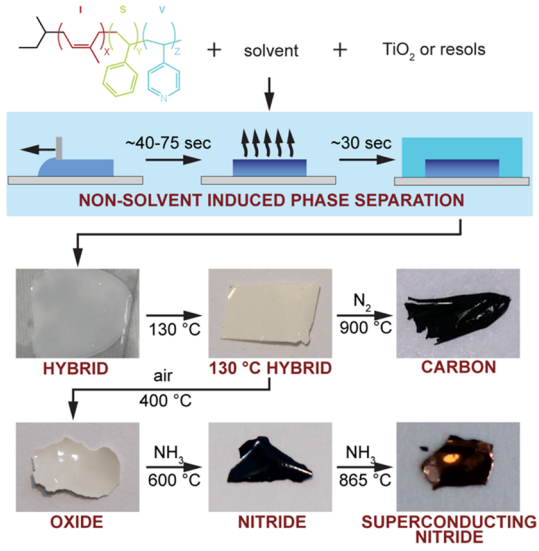

Figure 1. Schematic representation of the SNIPS process and heat-treatment. The casting solution, consisting of the ISV terpolymer mixed with either TiO_2 sol NPs or resols, was cast onto glass slides to form ≈200 to 400 μm thick films. After allowing the films to partially evaporate to induce an ISV+additive concentration gradient, they were plunged into a DI water bath, precipitating the polymer and converting the concentration gradient into an asymmetric composite structure. The resulting membranes were dried at RT and 130 °C. The ISV+resols hybrids were heated to 900 °C in inert atmosphere (N_2), leading to ISV decomposition and resulting in graphitic carbon. The ISV+TiO_2 hybrids were heat-treated in air (400 °C). This led to polymer decomposition and formation of freestanding anatase titanium(IV) oxide. The oxide was then subjected to heat-treatment in ammonia (600 °C) to form TiN. A second heat-treatment in ammonia (865 °C) led to superconducting TiN. Photographs of the materials at each synthetic step are shown at the bottom.

Briefly, an amphiphilic triblock terpolymer poly(isoprene)-*block*-poly(styrene)-*block*-poly(4-vinylpyridine) (ISV) was used to structure-direct either sol−gel-derived inorganic titanium dioxide (TiO_2) nanoparticles (NPs) or organic phenol formaldehyde resols (resols). The inorganic/organic additive preferentially swells the hydrophilic V block of ISV.[21,22] ISV was synthesized *via* sequential anionic polymerization.[23] For the nitrides, an ISV of molar mass 113 kg mol^{-1} with volume fractions of 29% poly(isoprene) (PI), 59% poly(styrene) (PS), and 12% poly(4-vinylpyridine) (P4VP) and dispersity ($Đ$) of 1.3 was used, while for the graphitic carbons, a different ISV of molar mass 95 kg mol^{-1}, volume fractions of 29% PI, 57% PS, and 14% P4VP, and $Đ$ = 1.2 was

https://dx.doi.org/10.1021/acsnano.0c05903
ACS Nano XXXX, XXX, XXX−XXX

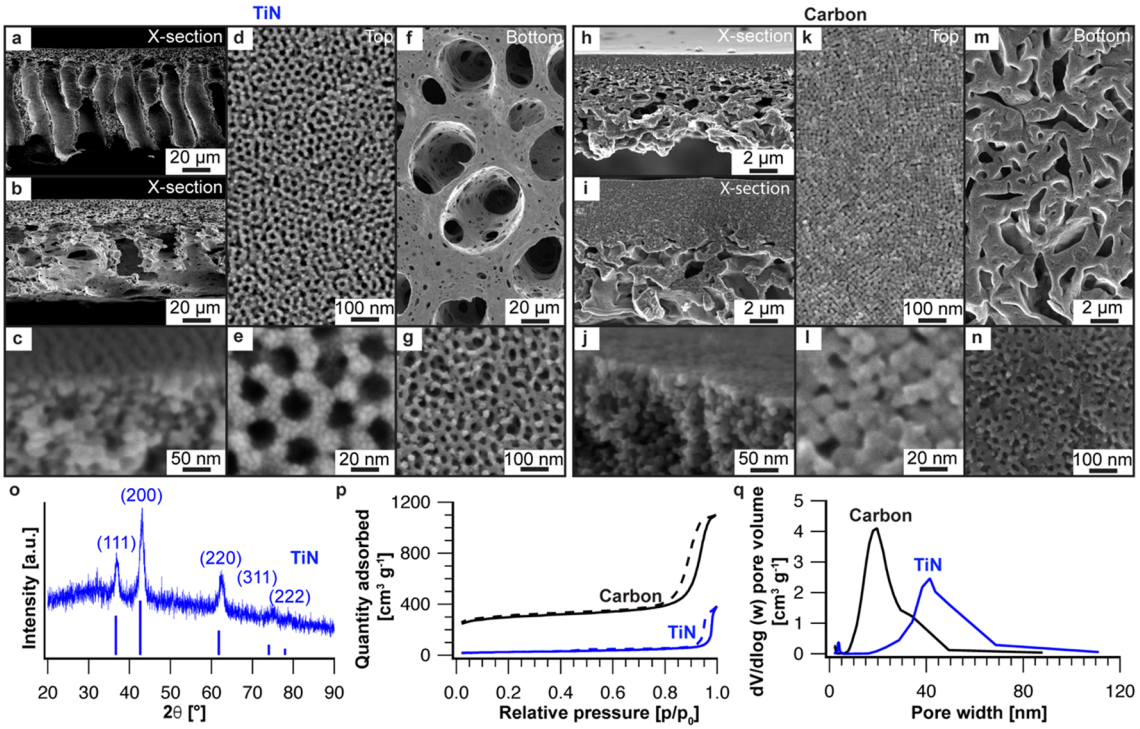

Figure 2. Characterization of asymmetric TiN and carbon. SEM characterization of (a–g) asymmetric TiN: (a, b) two different types of asymmetric TiN cross sections; (c) the top ≈150 nm mesoporous part of the cross-section; (d, e) the mesoporous top surface; (f) the bottom surface showing macropores; (g) the mesoporous wall. SEM characterization of (h–n) asymmetric carbon: (h, i) two different types of asymmetric carbon cross sections; (j) the top ≈150 nm mesoporous part of the cross section; (k, l) the mesoporous top surface; (m) the bottom surface showing macropores; (n) the mesoporous wall. (o) XRD pattern of TiN. Blue tick marks indicate expected peak positions and relative intensities for cubic TiN ($Fm\bar{3}m$, space group #225, ICSD #00-038-1420). (p) Nitrogen sorption isotherms of TiN (blue) and carbon (black) materials. (q) BJH-derived pore size distributions of the TiN (blue) and carbon (black) materials.

used. The TiO_2 NPs were prepared from a modified hydrolytic sol–gel synthesis, while resols were synthesized *via* condensation of phenol and formaldehyde under basic conditions.[24−26]

Solutions consisting of homogeneous mixtures of ISV and either TiO_2 NPs or resols dissolved in a mixture of 1,4-dioxane (DOX) and tetrahydrofuran (THF) (mass ratio of 7:3 DOX:THF) were cast onto glass slides using a doctor blade with a predetermined gate height on the order of a few hundred micrometers. Films were allowed to evaporate for a set amount of time *via* the film surface, which introduced an ISV+additive concentration gradient along the film normal. Evaporation was halted by plunging the films into deionized (DI) water (a nonsolvent for the polymer) to precipitate ISV, thus freezing in the asymmetric structure and resulting in an as-made ISV+TiO_2 hybrid or ISV+resols hybrid (Figure S1a and b, respectively). Subsequent drying and heat-treatments, first at 130 °C (Figure S1c and d, as well as Figure S1e, which is a representative XRD of the ISV+TiO_2 hybrid treated at 130 °C) and then higher temperatures as shown in Figure 2, converted the as-made composite materials into the final asymmetric inorganic porous structures.

Following heat-treatment at 130 °C, ISV+TiO_2 hybrids were heated to 400 °C in air for 3 h to remove organic material and produce porous freestanding asymmetric TiO_2 without loss of the asymmetric structure. Scanning electron microscopy (SEM), X-ray diffraction (XRD), and nitrogen sorption data for a representative material are provided in Figure S2. XRD peaks (Figure S2g) were consistent with anatase phase TiO_2 (ICSD #01-070-7348, space group #141 $I4_1/amd$) with lattice parameters of $a = b = 3.79$ Å and $c = 9.52$ Å and a coherent scattering domain size of 12.1 nm. These lattice parameters are comparable to those reported for bulk anatase TiO_2 ($a = b = 3.785$ Å, $c = 9.514$ Å),[27] while the domain size is on the order of the top surface strut thickness. Results of the nitrogen sorption and XRD characterization for all materials in this study are summarized in Tables S1 and S2, respectively. The oxide was converted into free-standing TiN by heat-treatment to 600 °C in flowing ammonia for 6 h before allowing the sample to cool to room temperature. For asymmetric carbon, heat-treatment at 130 °C of casted ISV+resols membranes induced cross-linking of the oligomeric resols. ISV+resols hybrids were subsequently heated to 900 °C in flowing nitrogen, decomposing the polymer and producing free-standing asymmetric carbon membranes.

Characterization of the final TiN and carbon structures *via* SEM, XRD, and nitrogen sorption is shown in Figure 2. By varying dope solution parameters, *e.g.*, film thickness and/or evaporation time, the cross sections and thereby surface area accessibility of the materials could be tuned. For TiN, gate heights of 305 to 381 μm and evaporation times of 60 s resulted in asymmetric cross sections with fingerlike profiles (Figure 2a). An increased evaporation time of 75 s resulted in denser cross sections with larger diameter macropores (Figure 2b), as increased solvent evaporation leaves behind a higher concentration film for precipitation. The final asymmetric TiN was considerably thinner (≈60 μm) than the original hybrid (≈100 μm, Figure S1), due to the mass loss during the decomposition of the organics. Asymmetric carbon products had thinner cross sections (≈8 μm) due to smaller casting gate

https://dx.doi.org/10.1021/acsnano.0c05903
ACS Nano XXXX, XXX, XXX–XXX

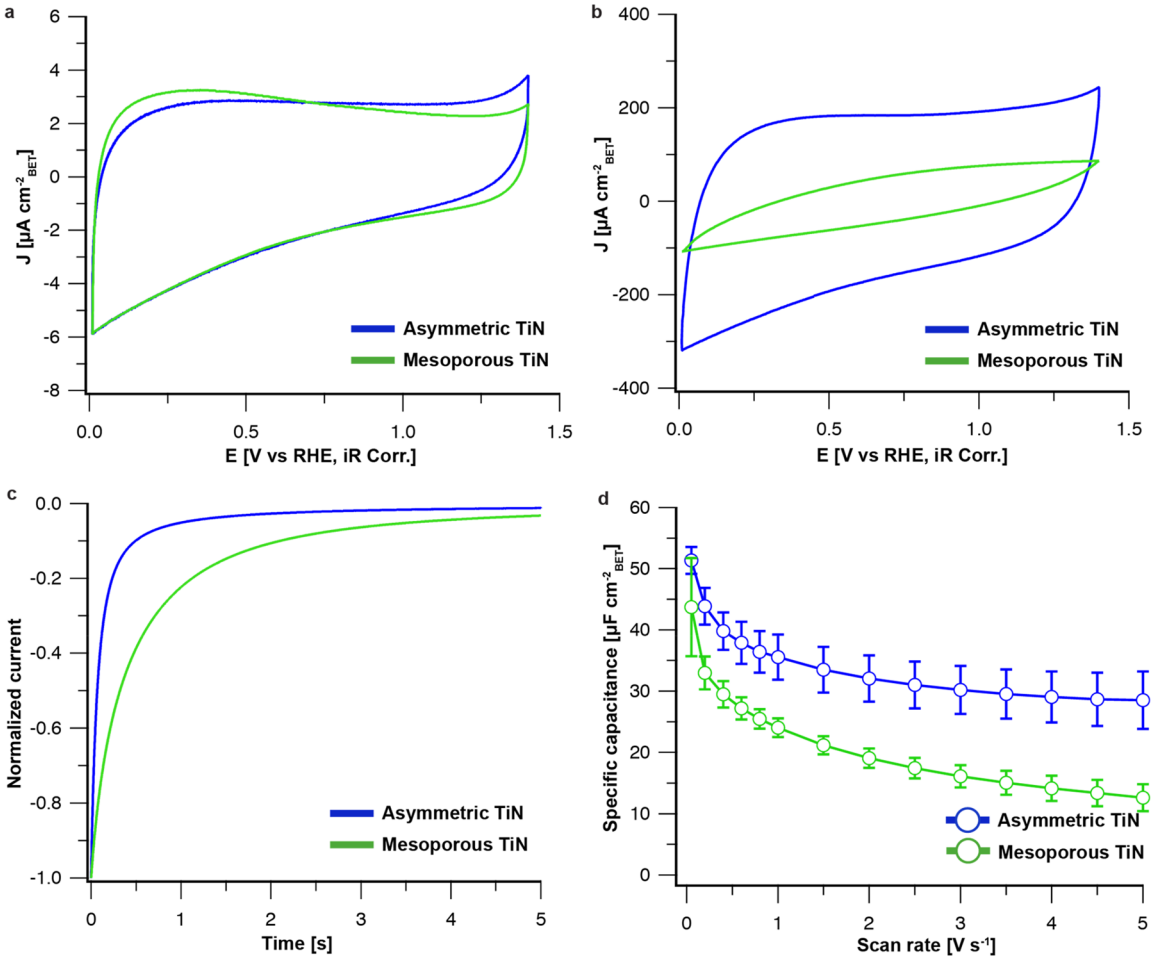

Figure 3. Electrochemical characterization of asymmetric TiN and gyroidal mesoporous TiN. Cyclic voltammograms for asymmetric TiN (blue) and mesoporous TiN (green) at (a) 50 mV s^{-1} and (b) 5 V s^{-1}. (c) Chronoamperometry starting from the open-circuit voltage to 0.01 V *vs* RHE showing enhanced ion diffusion in asymmetric TiN. (d) Scan rate dependence of specific capacitance for asymmetric TiN (blue) and mesoporous TiN (green) showing improved surface accessibility for asymmetric TiN. Error bars represent the standard deviation of three independent trials. All results were collected in Ar-saturated 0.1 mol L^{-1} $HClO_4$.

heights of 203 to 229 μm. By varying the solution preparation (simultaneous *vs* consecutive, see Materials and Methods section and Supporting Information (SI)), cross sections could be varied from a more asymmetric structure with a continuous gradient along the film normal (Figure 2h) to one with a denser top layer atop a macroporous substructure (Figure 2i).

Characterization details of the TiN sample in Figure 2b are provided in Figure 2c–g and o–q, while those of the sample depicted in Figure 2a are provided in Figure S3a–f and m. Similarly, details of the carbon sample whose cross section is shown in Figure 2i is provided in Figure 2j–n and p,q, while those of the sample shown in Figure 2h are provided in Figure S3g–l and n,o. The top ≈150 nm of the cross sections for both TiN and carbon asymmetric structures (Figure 2c and j) showed evidence of well-defined nanoscopic mesopores and nanoscale periodic ordering. For TiN, surface pores were arranged in a hexagonal structure (Figure 2d and e), consistent with the ISV+TiO_2 hybrid (Figure S1). For asymmetric carbon, the top surface showed a square pore arrangement (Figure 2k,l), reflecting the cubically packed pores of the hybrid material (Figure S1). For both TiN (Figure 2f) and carbon (Figure 2m), bottom surfaces exhibited micron-sized macropores. Furthermore, for both materials the walls of the macropores showed well-defined mesopores (Figure 2g,n), contributing to the specific surface area (*vide infra*). In summary, imaging results on these materials reveal an asymmetric pore structure, with well-defined mesopores at the top and macropores at the bottom, constituting a pore hierarchy. In addition to this asymmetry, throughout the material the macropore walls show well-defined mesopores, likely the result of the BCP SA process, which sequesters the inorganic precursors into nanoscopic domains everywhere along the film normal.[28,29]

XRD characterization of the TiN (Figure 2o) was consistent with cubic rocksalt TiN (ICSD #00-038-1420), which crystallized in space group $Fm\bar{3}m$ (#225) with a lattice parameter of 4.20 Å and a coherent scattering domain size of 6.9 nm. The lattice parameter is below the reported literature values, which lie between 4.235 and 4.242 Å,[30,31] but comparable to previously reported BCP-derived mesoporous TiN.[20] We attribute this difference to residual oxygen content and vacancies as described in previous studies.[30,32,33]

The porosity of asymmetric TiN and carbon samples was characterized *via* nitrogen sorption isotherms analyzed using the Brunauer–Emmett–Teller (BET) method (Figure 2p). In both cases, type-IV curves with H_1-type hysteresis and sharp capillary condensation above relative pressures of 0.99 were observed. For TiN, a BET surface area of (90 ± 3.0) m^2 g^{-1},

https://dx.doi.org/10.1021/acsnano.0c05903
ACS Nano XXXX, XXX, XXX–XXX

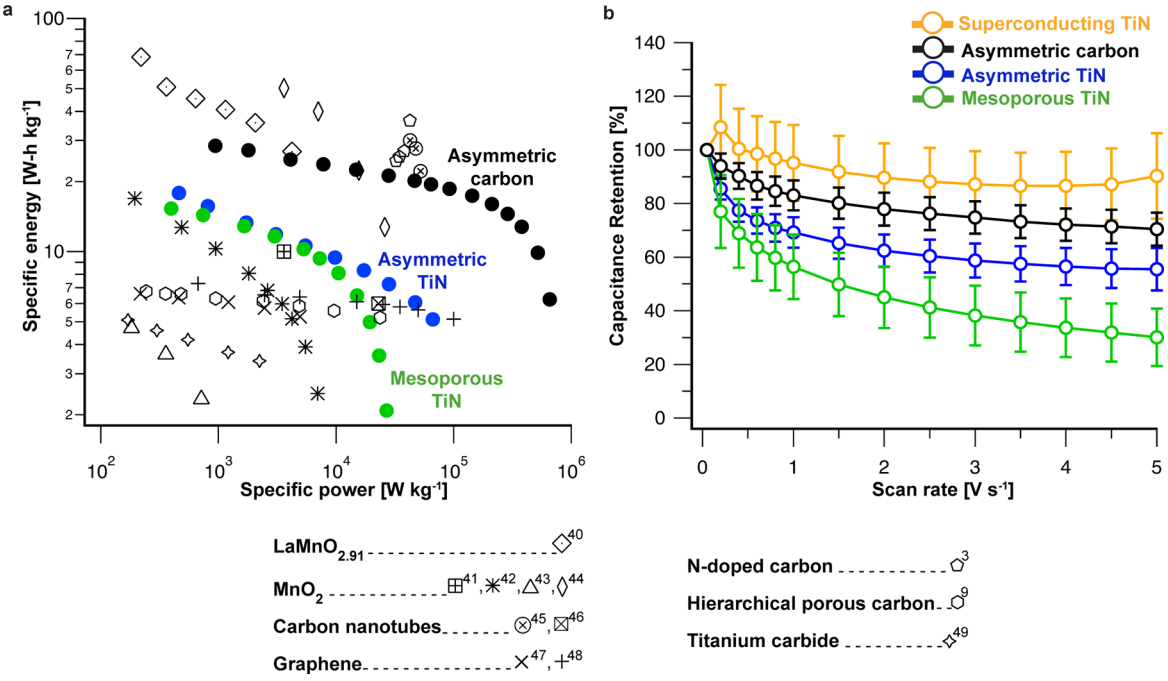

Figure 4. Capacitor performance benchmark and comparison of scan-rate-dependent capacitance retention. (a) Ragonne plot comparing energy storage performance of gyroidal mesoporous TiN, asymmetric TiN, and asymmetric carbon. Literature examples include $LaMnO_{2.91}$,[40] MnO_2,[41−44] carbon nanotubes,[45,46] graphene,[47,48] N-doped carbon,[3] hierarchical porous carbon,[9] and titanium carbide.[49]. (b) Scan rate dependence of capacitance retention for superconducting asymmetric TiN, asymmetric carbon, asymmetric TiN, and gyroidal mesoporous TiN. Error bars represent the standard deviation of three independent trials. All results were collected in Ar-saturated 0.1 mol L^{-1} $HClO_4$.

micropore area of 15 m^2 g^{-1}, volumetric surface area of 14.2 m^2 cm^{-3}, and specific pore volume of 0.59 cm^3 g^{-1} at p/p_0 = 0.99 were obtained. The reported errors result from the standard deviation from weighing each material several times. This surface area is similar to previously reported surface areas for mesoporous TiN, consistent with the mesoporous walls of the asymmetric material (*vide supra*).[20] Barrett−Joyner−Halenda (BJH) analysis (Figure 2q) revealed a well-defined pore size distribution that peaked at 41 nm with a full width at half-max (fwhm) of (17 ± 7) nm, similar to the oxide precursor (Figure S2i). The standard deviation of the fwhm is a result of fitting the pore size distribution to a Gaussian function with a least-squares fit. In comparison, asymmetric carbon had a much higher surface area due to increased microporosity and lower density. A BET surface area of (1024 ± 142) m^2 g^{-1}, micropore area of 655 m^2 g^{-1}, volumetric surface area of 36.0 m^2 cm^{-3}, and specific pore volume of 1.69 cm^3 g^{-1} at p/p_0 = 0.99 were obtained. BJH analysis (Figure 2q) showed a well-defined pore size distribution that peaked at 20 nm with a fwhm of (12 ± 5) nm. For an in-depth discussion of the microporosity features in such BCP-directed materials we refer to our earlier study.[24,34]

Gyroidal Mesoporous TiN Synthesis and Characterization. To evaluate ionic diffusion inside the asymmetric morphology, we compared the electrochemical performance of asymmetric TiN to homogeneous mesoporous TiN with the most accessible mesopores, *i.e.*, the three-dimensional alternating gyroid structure with interconnected pores.[24,26,34] Gyroidal mesoporous TiN was synthesized using evaporation-induced BCP-directed self-assembly (EISA) to closely match features of the asymmetric TiN in terms of thickness, pore size distribution, and specific surface area (see Materials and Methods section and SI). The ordered nanostructure was confirmed using small-angle X-ray scattering (SAXS) and SEM (Figure S4). The SAXS pattern could be indexed to an alternating gyroid ($I4_132$, space group #214) structure with unit cell size of 38 nm. The porosity was characterized using nitrogen sorption. Type-IV curves with H_1-type hysteresis and sharp capillary condensation above relative pressures of 0.99 were observed. A BET surface area of 139 m^2 g^{-1} with a weighing error of ±2.1 m^2 g^{-1}, micropore area of 34 m^2 g^{-1}, volumetric surface area of 108 m^2 cm^{-3}, and specific pore volume of 1.29 cm^3 g^{-1} at p/p_0 = 0.99 were observed with a peak in the pore size distribution around 24 nm with a fwhm of 4.2 nm, consistent with SEM results (Figure S4b,c). From pore size distribution analysis, pores of the gyroidal mesoporous TiN were on average slightly smaller than those of the asymmetric TiN. Further, the BET surface area of the mesoporous TiN was higher (139 m^2 g^{-1} *vs* 90 m^2 g^{-1}). XRD suggested mesoporous TiN crystallized with a rocksalt structure (ICSD #00-038-1420) and a lattice parameter of 4.20 Å with a coherent scattering domain size of 5.5 nm, similar to the asymmetric TiN.

Electrochemical Characterization of Asymmetric Structures. Cyclic voltammetry (CV) was conducted in aqueous 0.1 mol L^{-1} $HClO_4$ to compare ion diffusion in the asymmetric TiN monolith with gyroidal mesoporous TiN. Measured currents were normalized to the respective BET surface areas to obtain the capacitive response of the asymmetric and mesoporous TiN per their internal surface areas. At slow scan rates (50 mV s^{-1}), CVs of both morphologies showed similar capacitive current and specific integral capacitance, indicating that the internal pores were accessible at slow scan rates. In this limit, the internal ion diffusion is sufficiently fast with respect to the charge/discharge rate (Figure 3a). At high scan rates (5 V s^{-1})

https://dx.doi.org/10.1021/acsnano.0c05903
ACS Nano XXXX, XXX, XXX−XXX

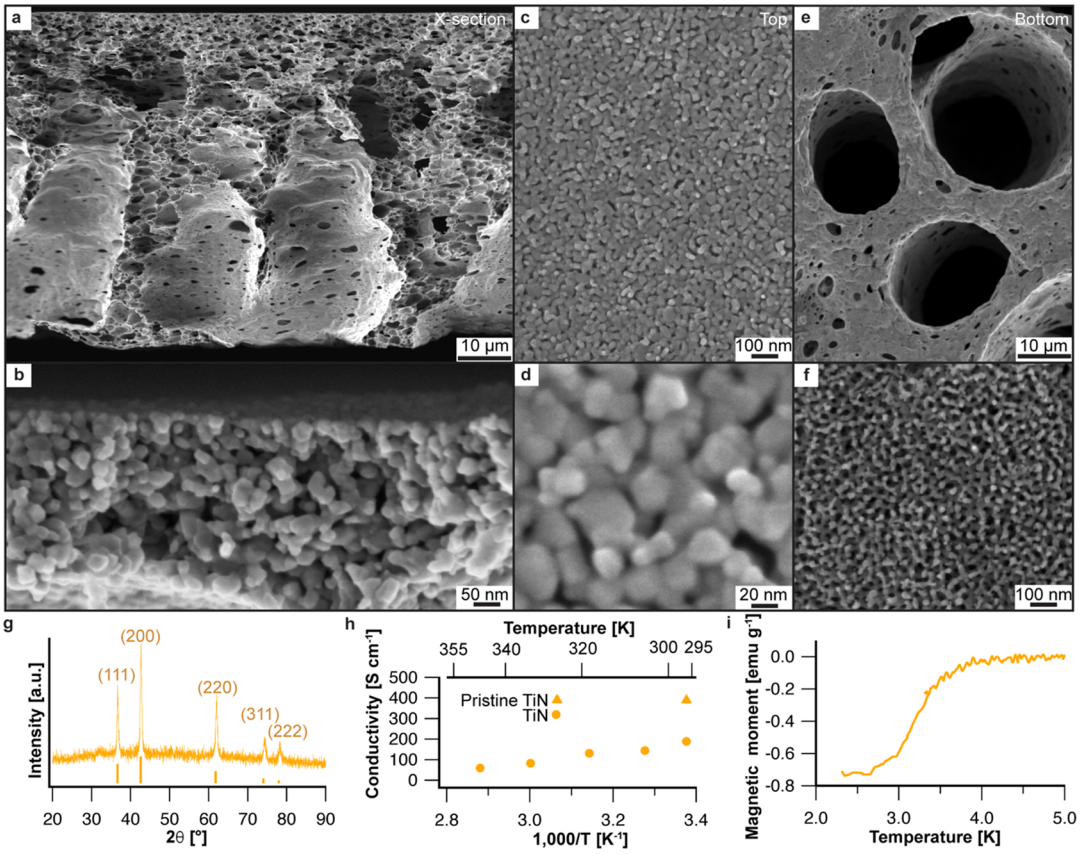

Figure 5. Characterization of asymmetric TiN superconductor. SEM characterization of (a) ≈50 μm thick asymmetric cross section; (b) the mesoporous top surface part of the cross section; (c, d) mesoporous top surface; (e) bottom surface with macropores; (f) mesoporous wall. (g) XRD pattern: Yellow tick marks indicate expected peak positions and relative intensities for cubic TiN (ICSD #00-038-1420). (h) Temperature-dependent conductivity measurements. TiN is a nitride sample that was exposed to air for a longer period of time than the pristine TiN. The lower conductivity relative to the pristine TiN sample suggests growth of a thin surface oxide layer. (i) Temperature-dependent magnetization from 2.2 to 5 K for a superconducting TiN membrane with an onset T_c of 3.8 K.

corresponding to charge/discharge in <0.3 s, however, the capacitive performance of the two morphologies diverged substantially (Figure 3b). While the CV for asymmetric TiN showed a similar shape to the one at slower scan rate, mesoporous TiN showed substantial integral capacitance loss (56% *vs* ≈30% initial value retention, see Figures 3d and 4b). We note that because mesoporous TiN had a higher BET surface area than the asymmetric TiN, the gravimetric (mass-normalized) integral capacitance was higher at slow scan rate; however, the trend was reversed at higher scan rate because the asymmetric TiN has a better rate capability (2× at 5 V s^{-1}, see Figures S5 and S6). To allow a fair comparison of surface area accessibility in asymmetric and mesoporous TiN, the solution resistance was corrected using the high-frequency intercept from impedance measurements and compensated (since the absolute surface areas of the two morphologies were not the same). The trend of improved integral capacitance retention in the asymmetric structure persisted even if we did not apply this correction (Figure S7).

To understand the origin of the capacitance retention in asymmetric TiN, chronoamperometry (CA) was used (Figure 3c). In this experiment, the voltage was held at the open-circuit voltage (≈0.65 to 0.75 V *vs* reversible hydrogen electrode (RHE)) for 5 min; then the potential was immediately dropped to 0.01 V *vs* RHE while the decay current was measured. After normalizing the maximum current to unity, we calculated effective time constants of 92.8 ms (asymmetric TiN) and 372 ms (mesoporous TiN), indicating that double-layer charging is approximately four times faster in the asymmetric structure, which we attribute to more facile ion diffusion in asymmetric TiN. This result is consistent with the improved capacitance retention for asymmetric TiN at higher scan rate. We note that the open-circuit voltage varied by <0.1 V between the asymmetric and mesoporous morphologies, consistent with the idea that the two structures had similar surface chemistries.

To demonstrate that SNIPS-derived asymmetric structures can also enhance mass transport through membranes with substantial microporosity, in addition to mesoporosity, we measured the rate-dependent integral capacitance of asymmetric graphitic carbon. Due to the microporosity in asymmetric carbon, the specific surface area is an order of magnitude higher than asymmetric TiN, potentially allowing higher power and energy densities. However, the ability to access a high fraction of the fine <2 nm micropores at fast rates is critical. To remove organic impurities and increase the capacitance, the asymmetric carbon was first activated by cycling to 1.4 V *vs* RHE at 5 V s^{-1}. We note that this step will likely also introduce redox functional groups, *e.g.*, oxygen on the carbon surface. Like asymmetric TiN, the CV retained most of the low scan rate features even at a relatively fast 5 V s^{-1} scan rate (Figure S8a). The CVs shown in Figure S8a were measured using the same protocol as for TiN after the activation step had reached a steady-state CV shape and

https://dx.doi.org/10.1021/acsnano.0c05903
ACS Nano XXXX, XXX, XXX−XXX

capacitive current. We found the specific integral capacitance of asymmetric carbon to be 13.8 μF cm$^{-2}_{BET}$ at 50 mV s^{-1}, normalized using the BET-derived surface area, with 70% capacity retention at 5 V s^{-1}, suggesting that in addition to the mesopores a high fraction of the micropores remain accessible at fast rates.

We attribute the high capacitance retention performance of the asymmetric structure to the improved pore accessibility at high rates (Figure 4b). To illustrate the benefit of the asymmetric architecture, the energy density and power density of asymmetric and gyroidal mesoporous TiN and asymmetric graphitic carbon were calculated and compared to state-of-the-art literature values (Figure 4a, Table S3). We report gravimetric energy and power densities of a single electrode using a three-electrode half-cell configuration. In order to provide a fair comparison, in the SI (Table S3) details of our calculations are compared to those described in the prior literature and leading to each of the reference points shown in Figure 4a. Since most literature reports do not include resistance compensation, we report energy and power density values without resistance compensation. Full calculation details are included in the SI. Electrode thicknesses are reported in Table S4. Due to the facile ion diffusion through the asymmetric structure, which leads to capacitance retention at high scan rates, the peak average power density for both asymmetric structures of TiN (28.2 kW kg^{-1}) and graphitic carbon (287.9 kW kg^{-1}) are substantially higher than the state of the art. The energy density at the peak power density for TiN is 7.3 W-h kg^{-1} and for graphitic carbon is 14.5 W-h kg^{-1}. We attribute the higher energy density in carbon to the higher micropore surface area compared to TiN. At the measured power density, as well as all power densities greater than 100 kW kg^{-1}, these energy density values are among the highest energy values reported to date, including reports utilizing purely asymmetric/hierarchical or mesoporous structures, suggesting that the combination of structural asymmetry with well-defined mesopores and micropores throughout the material is an important structural aspect resulting in improved performance.[9] We stress that these values represent a nonoptimized result. We expect further improvements can be made by adding additional functional groups such as amines or by activating the carbon with CO_2 to further increase microporosity and surface area or by incorporating more conductive materials (*vide infra*).[35] Furthermore, the SNIPS process could be further optimized to improve capacitance retention, power density, and energy density.

Electrical Conductivity Limitations on Capacitance Retention. Given the record-setting power performance of the studied asymmetric structures, we tested whether the obtained result represents the fundamental limit of transport inside the porous structures. One of the possible limitations of our porous structures is the reduced electrical conductivity in TiN. To test the influence of electrical conductivity, we examined the rate capability of the asymmetric TiN with less residual oxygen, which has improved electrical conductivity. To this end, we used a second heat-treatment step under flowing NH_3 to remove residual lattice oxygen and vacancies. After initial annealing at 600 °C for 6 h, asymmetric TiN monoliths were subsequently annealed under flowing NH_3 at 865 °C for 3 h. After annealing, the structure retained its asymmetric morphology (Figure 5a,b), with open and accessible macroporous bottom and mesoporous walls (Figure 5e,f). The ordered top surface densified, however, likely a result of crystallite overgrowth (Figure 5c,d). Importantly, while the XRD peaks and relative intensities (Figure 5g) remained consistent with cubic rocksalt TiN (ICSD #00-038-1420), the lattice parameter from XRD increased from 4.20 Å to 4.24 Å, similar to bulk TiN and suggesting removal of additional residual oxygen/vacancies.[30,31] Furthermore, the grain size increased from 6.9 nm to 19 nm, consistent with the size of domains observed on the top surface in SEM (*e.g.*, Figure 5d). The progression of the transformation through various processing steps is shown in Figure S9.

The annealed membrane had a conductivity of 188 S cm^{-1} with a temperature-dependent behavior consistent with metallic conductivity (Figure 5h) measured using a four-point probe geometry (Figure S10), comparable to that of glassy carbon and BCP-derived porous TiN thin films.[20,36] While this electrical conductivity is sufficient for electrochemical testing, the value is lower than that for bulk TiN (>10^4 S cm^{-1}) likely due to the remaining residual oxygen and vacancies resulting from the low ammonolysis temperature needed to maintain the porous structure as well as a thin surface oxide layer that forms upon longer exposure of the material to air (see Figure 5h). In addition, the nanoscale grain sizes can also increase electron scattering, lowering conductivity.[32,37]

One signature of significantly reduced oxygen defects in TiN is the presence and temperature of a superconducting transition. A superconducting membrane could be applied, for example, in magnetic gas separations.[38] To probe the superconducting transition in these materials, the temperature-dependent magnetization of the high-temperature-annealed asymmetric TiN was measured under an applied field of 796 A m^{-1} during warming after zero-field cooling to 2.5 K (Figure 5i). A superconducting transition was observed between 2.5 K and about 4 K, with a flux expulsion from the material indicated by negative values of the magnetic moment. The observed T_c (3.8 K) is slightly below the value reported in the literature for TiN (5.6 K), possibly due to residual oxygen and vacancies in the lattice.[30,32,33]

To study the effect of residual oxygen content on the electrochemical properties of asymmetric TiN, the capacitance retention of the reannealed TiN was investigated using CV. Like the previous TiN monolith, a double-layer capacitance response dominated the CV result when scanned between 50 mV s^{-1} and 5 V s^{-1}. The measured capacitive current was lower than the previous TiN monolith (Figure S11a,b). We attribute this observation to the loss of residual oxygen, which could be redox-active and thus can contribute an additional capacitive response.[39] More importantly, the capacitance retention (Figure 4b) at 5 V s^{-1} was 90% with respect to the slow scan rate integral capacitance, substantially higher than the 56% retention measured for the asymmetric TiN treated at only 600 °C (see also Figure S11c). At slow scan rates, we cannot rule out the possibility that kinetically slow pseudocapacitance derived from the redox sites in asymmetric TiN contributes to the reduced capacitance retention *vs* superconducting TiN. However, the capacitance retention trend for faster scan rates (500 mV s^{-1} to 5 V s^{-1}) is similar, suggesting that improved electrical conductivity is the dominant factor. On the basis of this result, we conclude that our experiment does not yet test the limit of diffusion inside the asymmetric TiN structure. Instead, the limitation of our measurement is likely the electrical conductivity of the synthesized material.

https://dx.doi.org/10.1021/acsnano.0c05903
ACS Nano XXXX, XXX, XXX−XXX

CONCLUSIONS

Our results suggest that membrane materials combining asymmetric (hierarchical) pore morphologies with well-defined mesoporosity throughout the material, as derived from a combination of NIPS and BCP self-assembly, have superior diffusional performance and pore utilization compared to membrane materials that have either only asymmetric (hierarchical) pore structures or well-defined mesopores. Using this realization, we were able to improve the energy and power densities of both TiN- and carbon-based electrochemical double-layer capacitors beyond the highest values reported to date. Our fabrication method can be readily applied to other inorganic additives, enabling a whole library of inorganic membrane materials combining asymmetric pore structures with well-defined mesoporosity. Together with the industry-proven and scalable formation process, our work provides an advanced approach for tailoring future porous materials for energy storage and conversion devices as well as other applications in the area of sustainability.

MATERIALS AND METHODS

Materials Synthesis/Preparation. *Asymmetric TiN Synthesis.* Asymmetric TiO_2 and TiN were synthesized *via* block copolymer self-assembly and non-solvent-induced phase separation using poly(isoprene-*b*-styrene-*b*-4-vinylpyridine) (PI-*b*-PS-*b*-P4VP, or simply ISV) triblock terpolymers with sol–gel-derived TiO_2 nanoparticles. The ISV polymer had a molar mass of 113 kg mol^{-1} with volume fractions of 29% PI, 59% PS, and 12% P4VP, and a dispersity of 1.3. TiO_2 nanoparticles were synthesized *via* a hydrolytic sol–gel process and added to an ISV polymer dissolved in DOX and THF at a mass ratio of 7:3 DOX:THF (see Supporting Information for details). After stirring, the casting solution was pipetted onto a glass substrate, and a thick film was cast with a doctor blade. After either 60 or 75 s evaporation time, to allow for the formation of a concentration gradient along the film-normal, the films were plunged into a nonsolvent DI water bath to allow for precipitation, producing porous hybrid membranes with a structural gradient.

Monoliths were dried at 50 °C for 2 h and 130 °C for 5 h. Subsequently, the hybrid monoliths were heated at 400 °C for 3 h to remove the polymer template and then at 600 °C for 6 h under flowing NH_3 (10 L h^{-1}) to form the final nitride. Superconducting TiN was obtained using a second heat-treatment in NH_3 (10 L h^{-1}) at 865 °C for 3 h.

Asymmetric Carbon Synthesis. Asymmetric carbon was synthesized using a similar SNIPS process with an ISV triblock terpolymer and phenol formaldehyde resols synthesized *via* condensation of phenol and formaldehyde under basic conditions (see SI for details). The ISV polymer used had a molar mass of 95 kg mol^{-1} with volume fractions of 29% PI, 57% PS, and 14% P4VP and a dispersity of 1.2. Precursor hybrid polymer/resol solutions were made using two processes. In the first, "consecutive", method the ISV polymer was dissolved in a mixture of DOX and THF at mass ratio of 7:3 DOX:THF followed by addition of the resol solution in the same solvent mixture, while in the "simultaneous" method the solid ISV polymer was added directly to the resol solution. After stirring, the hybrid solutions were pipetted onto a glass substrate at 30 °C, and a doctor blade was used to form a thick film. After 40 s evaporation time to allow formation of the concentration gradient, the films were plunged into a nonsolvent DI water bath.

Monoliths were dried at 50 °C for 2 h and 130 °C for 5 h. Subsequently, the hybrid monoliths were heated at 600 °C for 3 h under flowing N_2, followed by further heating at 900 °C for 3 h.

Gyroidal Mesoporous TiN Synthesis. Alternating gyroid mesoporous TiN was synthesized *via* block copolymer self-assembly using poly(isoprene-*b*-styrene-*b*-ethylene oxide) (PI-*b*-PS-*b*-PEO, or simply ISO) with sol–gel-derived TiO_2 nanoparticles (see SI for details). The ISO polymer was synthesized *via* sequential living anionic polymerization and had a molar mass of 83 kg mol^{-1} with volume fractions of 29% PI, 64% PS, and 6.5% PEO and a dispersity of 1.09. TiO_2 nanoparticles were synthesized *via* a hydrolytic sol–gel process and mixed with ISO dissolved in THF. After stirring, the nanoparticle/polymer hybrid solution was cast in a Teflon dish under a glass dome and dried at room temperature, allowing EISA. After self-assembly, the polymer/nanoparticle hybrid monoliths were further dried at 50 °C for 2 h and 130 °C for 5 h. Dense interface overlayers were removed by etching with CF_4 plasma at 300 W for 45 min on each side of the film. Subsequently, the hybrid monoliths were heated at 400 °C for 3 h in air to remove the polymer template and then at 600 °C for 6 h under flowing NH_3 (10 L h^{-1}) to form the final nitride.

Materials Characterization. SEM micrographs were obtained using a ZEISS Gemini 500 SEM operated at an accelerating voltage of 2 kV. Samples were either uncoated or coated with gold–palladium prior to imaging. XRD data for the hybrids, oxides, and nitrides were collected on a Bruker D8 Advance ECO powder diffractometer equipped with a high-speed silicon strip detector, using Cu Kα radiation (λ = 1.54 Å) and a step size of 0.019° (2θ) at 5.7° min^{-1}. Nitrogen adsorption–desorption isotherms of the oxides, nitrides, and carbons were recorded using a Micromeritics ASAP 2020 surface area and porosity analyzer at −196 °C. SAXS data were collected at the Soft Matter Interfaces beamline at NSLS-II in in-vacuum mode using a Dectris Pilatus 1M detector.

To measure electrical conductivity, gold contact pads were sputter deposited on the nitride monoliths and a silver wire was connected using silver epoxy. Conductivity measurements were subsequently performed using the four-point van der Pauw method. Temperature-dependent magnetization measurements were conducted on a Quantum Design Physical Property Measurement System (PPMS) Vibrating Sample Magnetometer (VSM).

Electrodes were fabricated by adhering a titanium wire to the nitride and carbon monoliths with gold paint and subsequently covering both the gold paint and wire with a chemically inert epoxy. All electrochemical measurements were conducted using a three-electrode cell with a 0.1 mol L^{-1} $HClO_4$ electrolyte, a platinum wire counter electrode, and a Ag/AgCl reference electrode. Capacitance measurements of all monoliths were obtained using cyclic voltammetry in Ar-saturated 0.1 mol L^{-1} $HClO_4$ both with and without *iR* drop correction. The total resistance, *R*, was measured as the AC impedance at high frequency in the three-electrode system and corresponded to the sum of all electrolyte and contact resistances. Chronoamperometry measurements were similarly conducted in Ar-saturated 0.1 mol L^{-1} $HClO_4$ using a three-electrode cell.

ASSOCIATED CONTENT

Supporting Information

The Supporting Information is available free of charge at https://pubs.acs.org/doi/10.1021/acsnano.0c05903.

Additional information (PDF)

AUTHOR INFORMATION

Corresponding Author

Ulrich Wiesner − *Department of Materials Science and Engineering, Cornell University, Ithaca, New York 14853, United States;* orcid.org/0000-0001-6934-3755; Email: ubw1@cornell.edu

Authors

Sarah A. Hesse − *Department of Materials Science and Engineering and Department of Chemistry and Chemical Biology, Cornell University, Ithaca, New York 14853, United States;* orcid.org/0000-0002-2383-4476

Kevin E. Fritz − *Department of Materials Science and Engineering, Cornell University, Ithaca, New York 14853, United States;* orcid.org/0000-0002-9033-8157

https://dx.doi.org/10.1021/acsnano.0c05903
ACS Nano XXXX, XXX, XXX−XXX

Peter A. Beaucage − *Department of Materials Science and Engineering, Cornell University, Ithaca, New York 14853, United States; Materials Science and Engineering Division, National Institute of Standards and Technology, Gaithersburg, Maryland 20899, United States;* orcid.org/0000-0002-2147-0728

R. Paxton Thedford − *Department of Materials Science and Engineering and Robert Frederick Smith School of Chemical and Biomolecular Engineering, Cornell University, Ithaca, New York 14853, United States;* orcid.org/0000-0003-0811-227X

Fei Yu − *Department of Materials Science and Engineering and Department of Chemistry and Chemical Biology, Cornell University, Ithaca, New York 14853, United States;* orcid.org/0000-0002-8191-8096

Francis J. DiSalvo − *Department of Chemistry and Chemical Biology, Cornell University, Ithaca, New York 14853, United States*

Jin Suntivich − *Department of Materials Science and Engineering and Kavli Institute for Nanoscale Science, Cornell University, Ithaca, New York 14853, United States;* orcid.org/0000-0002-3427-4363

Complete contact information is available at: https://pubs.acs.org/10.1021/acsnano.0c05903

Author Contributions

All authors have given approval to the final version of the manuscript.

Author Contributions

S.A.H., K.E.F., P.A.B., and U.B.W. conceived the project. S.A.H. performed and optimized synthesis and collected and analyzed SEM, N_2 sorption, and XRD data. K.E.F. collected and analyzed electrochemical data, supervised by J.S. F.J.D. and P.A.B. assisted with some XRD data analysis and some synthetic optimization. P.A.B. collected and analyzed low-temperature magnetization data. P.A.B. collected the SAXS data. R.P.T. collected and analyzed conductivity. F.Y. performed sample etching. U.W. supervised the work and helped interpret data. S.A.H., K.E.F., J.S., and U.B.W. wrote the manuscript with input from all authors.

Author Contributions

¶S. A. Hesse and K. E. Fritz contributed equally.

Notes

The authors declare the following competing financial interest(s): The authors declare that they have submitted a patent disclosure based on this study through Cornell University.

ACKNOWLEDGMENTS

This work was funded by the National Science Foundation under award DMR-1707836. K.E.F. and J.S. further thank the Center for Alkaline Based Energy Solutions (CABES), an Energy Frontier Research Center funded by the U.S. Department of Energy, Office of Science, Office of Basic Energy Sciences, under Award No. DE-SC0019445 (electrochemical characterization). This work made use of the Cornell Center for Materials Research (CCMR) Shared Facilities, which are supported through the NSF MRSEC program (DMR-1719875) and the Cornell NanoScale Science and Technology Facility (CNF), a member of the National Nanotechnology Coordinated Infrastructure (NNCI), which is supported by the NSF (Grant ECCS-15420819). This work made use of the NMR Facility at Cornell University, which is supported, in part, by the NSF under the award CHE-1531632. P.A.B. and R.P.T. were supported by the National Science Foundation Graduate Research Fellowship Program (DGE-1650441). This research used the Soft Matter Interfaces (SMI) beamline of the National Synchrotron Light Source II, a U.S. Department of Energy (DOE) Office of Science User Facility operated for the DOE Office of Science by Brookhaven National Laboratory under Contract No. DE-SC0012704. The authors thank S. M. Gruner for use of laboratory space and equipment for conductivity measurements, J. A. Hinckley for input on figure design, D.-Y. Kuo for discussions and advice on electrochemical measurements, and E. M. Susca for discussions of XRD and BET results. Certain commercial equipment, instruments, software, or materials are identified in this paper to foster understanding. Such identification does not imply recommendation or endorsement by the National Institute of Standards and Technology, nor does it imply that the materials or equipment identified are necessarily the best available for the purpose.

REFERENCES

(1) Bruce, P. G.; Scrosati, B.; Tarascon, J.-M. Nanomaterials for Rechargeable Lithium Batteries. *Angew. Chem., Int. Ed.* **2008**, *47*, 2930−2946.

(2) Sun, Y.; Liu, N.; Cui, Y. Promises and Challenges of Nanomaterials for Lithium-Based Rechargeable Batteries. *Nat. Energy* **2016**, *1*, 16071.

(3) Lin, T.; Chen, I.-W.; Liu, F.; Yang, C.; Bi, H.; Xu, F.; Huang, F. Nitrogen-Doped Mesoporous Carbon of Extraordinary Capacitance for Electrochemical Energy Storage. *Science* **2015**, *350*, 1508−1513.

(4) Miller, J. R.; Simon, P. Materials Science: Electrochemical Capacitors for Energy Management. *Science* **2008**, *321*, 651−652.

(5) Breitsprecher, K.; Holm, C.; Kondrat, S. Charge Me Slowly, I Am in a Hurry: Optimizing Charge-Discharge Cycles in Nanoporous Supercapacitors. *ACS Nano* **2018**, *12*, 9733−9741.

(6) Simon, P.; Gogotsi, Y.; Dunn, B. Where Do Batteries End and Supercapacitors Begin? *Science* **2014**, *343*, 1210−1211.

(7) Rolison, D. R.; Long, J. W.; Lytle, J. C.; Fischer, A. E.; Rhodes, C. P.; McEvoy, T. M.; Bourg, M. E.; Lubers, A. M. Multifunctional 3D Nanoarchitectures for Energy Storage and Conversion. *Chem. Soc. Rev.* **2009**, *38*, 226−252.

(8) Aricò, A. S.; Bruce, P.; Scrosati, B.; Tarascon, J.-M.; Van Schalkwijk, W. Nanostructured Materials for Advanced Energy Conversion and Storage Devices. *Nat. Mater.* **2005**, *4*, 366−377.

(9) Wang, D.-W.; Li, F.; Liu, M.; Lu, G. Q.; Cheng, H.-M. 3D Aperiodic Hierarchical Porous Graphitic Carbon Material for High-Rate Electrochemical Capacitive Energy Storage. *Angew. Chem., Int. Ed.* **2008**, *47*, 373−376.

(10) Kondrat, S.; Kornyshev, A. A. Pressing a Spring: What Does It Take to Maximize the Energy Storage in Nanoporous Supercapacitors? *Nanoscale Horizons* **2016**, *1*, 45−52.

(11) He, L.; Yang, L.; Dincă, M.; Zhang, R.; Li, J. Observation of Ion Electrosorption in Metal−Organic Framework Micropores with *in Operando* Small-Angle Neutron Scattering. *Angew. Chem., Int. Ed.* **2020**, *132*, 9773−9779.

(12) Janssen, M. Curvature Affects Electrolyte Relaxation: Studies of Spherical and Cylindrical Electrodes. *Phys. Rev. E: Stat. Phys., Plasmas, Fluids, Relat. Interdiscip. Top.* **2019**, *100*, No. 042602.

(13) AbdelAty, A. M.; Fouda, M. E.; Elbarawy, M. T. M. M.; Radwan, A. G. Optimal Charging and Discharging of Supercapacitors. *J. Electrochem. Soc.* **2020**, *167*, 110521.

(14) Ulbricht, M. Advanced Functional Polymer Membranes. *Polymer* **2006**, *47*, 2217−2262.

(15) Wu, Y.; Liu, Z.; Ran, F. New Comprehensions on Structure Superiority of Asymmetric Carbon Membrane and Controlled Construction of Advanced Hierarchical Inner-Structure for High

Performance Supercapacitors. *Microporous Mesoporous Mater.* **2019**, *275*, 14−25.
(16) Yang, X.; Chen, Y.; Wang, M.; Zhang, H.; Li, X.; Zhang, H. Phase Inversion: A Universal Method to Create High-Performance Porous Electrodes for Nanoparticle-Based Energy Storage Devices. *Adv. Funct. Mater.* **2016**, *26*, 8427−8434.
(17) Ran, F.; Shen, K.; Tan, Y.; Peng, B.; Chen, S.; Zhang, W.; Niu, X.; Kong, L.; Kang, L. Activated Hierarchical Porous Carbon as Electrode Membrane Accommodated with Triblock Copolymer for Supercapacitors. *J. Membr. Sci.* **2016**, *514*, 366−375.
(18) Peinemann, K.-V.; Abetz, V.; Simon, P. F. W. Asymmetric Superstructure Formed in a Block Copolymer *via* Phase Separation. *Nat. Mater.* **2007**, *6*, 992−996.
(19) Dorin, R. M.; Marques, D. S.; Sai, H.; Vainio, U.; Phillip, W. A.; Peinemann, K.-V.; Nunes, S. P.; Wiesner, U. Solution Small-Angle X-Ray Scattering as a Screening and Predictive Tool in the Fabrication of Asymmetric Block Copolymer Membranes. *ACS Macro Lett.* **2012**, *1*, 614−617.
(20) Fritz, K. E.; Beaucage, P. A.; Matsuoka, F.; Wiesner, U.; Suntivich, J. Mesoporous Titanium and Niobium Nitrides as Conductive and Stable Electrocatalyst Supports in Acid Environments. *Chem. Commun.* **2017**, *53*, 7250−7253.
(21) Weng, C.-C.; Hsu, K.-F.; Wei, K.-H. Synthesis of Arrayed, TiO_2 Needlelike Nanostructures *via* a Polystyrene-*Block*-Poly(4-Vinylpyridine) Diblock Copolymer Template. *Chem. Mater.* **2004**, *16*, 4080−4086.
(22) Lou, Q.; Chinthamanipeta, P. S.; Shipp, D. A. Mechanism of Titania Deposition into Cylindrical Poly(Styrene-*Block*-4 Vinyl Pyridine) Block Copolymer Templates. *Langmuir* **2011**, *27*, 15206−15212.
(23) Phillip, W. A.; Dorin, R. M.; Werner, J.; Hoek, E. M. V; Wiesner, U.; Elimelech, M. Tuning Structure and Properties of Graded Triblock Terpolymer-Based Mesoporous and Hybrid Films. *Nano Lett.* **2011**, *11*, 2892−2900.
(24) Werner, J. G.; Hoheisel, T. N.; Wiesner, U. Synthesis and Characterization of Gyroidal Mesoporous Carbons and Carbon Monoliths with Tunable Ultralarge Pore Size. *ACS Nano* **2014**, *8*, 731−743.
(25) Hesse, S. A.; Werner, J. G.; Wiesner, U. One-Pot Synthesis of Hierarchically Macro- and Mesoporous Carbon Materials with Graded Porosity. *ACS Macro Lett.* **2015**, *4*, 477−482.
(26) Robbins, S. W.; Sai, H.; DiSalvo, F. J.; Gruner, S. M.; Wiesner, U. Monolithic Gyroidal Mesoporous Mixed Titanium-Niobium Nitrides. *ACS Nano* **2014**, *8*, 8217−8223.
(27) Cromer, D. T.; Herrington, K. The Structures of Anatase and Rutile. *J. Am. Chem. Soc.* **1955**, *77*, 4708−4709.
(28) Hoheisel, T. N.; Hur, K.; Wiesner, U. B. Block Copolymer-Nanoparticle Hybrid Self-Assembly. *Prog. Polym. Sci.* **2015**, *40*, 3−32.
(29) Hur, K.; Wiesner, U. Design and Applications of Multiscale Organic-Inorganic Hybrid Materials Derived from Block Copolymer Self-Assembly. *Adv. Polym. Sci.* **2013**, *262*, 259−294.
(30) Hardy, G. F.; Hulm, J. K. The Superconductivity of Some Transition Metal Compounds. *Phys. Rev.* **1954**, *93*, 1004−1016.
(31) Kamiya, K.; Nishijima, T.; Tanaka, K. Nitridation of the Sol−Gel-Derived Titanium Oxide Films by Heating in Ammonia Gas. *J. Am. Ceram. Soc.* **1990**, *73*, 2750−2752.
(32) Robbins, S. W.; Beaucage, P. A.; Sai, H.; Tan, K. W.; Werner, J. G.; Sethna, J. P.; DiSalvo, F. J.; Gruner, S. M.; Van Dover, R. B.; Wiesner, U. Block Copolymer Self-Assembly-Directed Synthesis of Mesoporous Gyroidal Superconductors. *Sci. Adv.* **2016**, *2*, No. e1501119.
(33) Brauer, G. Nitrides, Carbonitrides and Oxynitrides of Niobium. *J. Less-Common Met.* **1960**, *2*, 131−137.
(34) Werner, J. G.; Rodríguez-Calero, G. G.; Abruña, H. D.; Wiesner, U. Block Copolymer Derived 3-D Interpenetrating Multifunctional Gyroidal Nanohybrids for Electrical Energy Storage. *Energy Environ. Sci.* **2018**, *11*, 1261−1270.
(35) Werner, J. G.; Johnson, S. S.; Vijay, V.; Wiesner, U. Carbon-Sulfur Composites from Cylindrical and Gyroidal Mesoporous Carbons with Tunable Properties in Lithium-Sulfur Batteries. *Chem. Mater.* **2015**, *27*, 3349−3357.
(36) Baker, D. F.; Bragg, R. H. The Electrical Conductivity and Hall Effect of Glassy Carbon. *J. Non-Cryst. Solids* **1983**, *58*, 57−69.
(37) Yang, M.; Cui, Z.; DiSalvo, F. J. Mesoporous Titanium Nitride Supported Pt Nanoparticles as High Performance Catalysts for Methanol Electrooxidation. *Phys. Chem. Chem. Phys.* **2013**, *15*, 1088−1092.
(38) Jang, E.-S.; Chang, J.-J.; Gwak, J.; Ayral, A.; Rouessac, V.; Cot, L.; Hwang, S.-J.; Choy, J.-H. Asymmetric High-T_c Superconducting Gas Separation Membrane. *Chem. Mater.* **2007**, *19*, 3840−3844.
(39) Choi, D.; Kumta, P. N. Synthesis and Characterization of Nanostructured Niobium and Molybdenum Nitrides by a Two-Step Transition Metal Halide Approach. *J. Am. Ceram. Soc.* **2011**, *94*, 2371−2378.
(40) Mefford, J. T.; Hardin, W. G.; Dai, S.; Johnston, K. P.; Stevenson, K. J. Anion Charge Storage through Oxygen Intercalation in $LaMnO_3$ Perovskite Pseudocapacitor Electrodes. *Nat. Mater.* **2014**, *13*, 726−732.
(41) Brousse, T.; Toupin, M.; Bélanger, D. A Hybrid Activated Carbon-Manganese Dioxide Capacitor Using a Mild Aqueous Electrolyte. *J. Electrochem. Soc.* **2004**, *151*, A614−A622.
(42) Lei, Z.; Zhang, J.; Zhao, X. S. Ultrathin MnO_2 Nanofibers Grown on Graphitic Carbon Spheres as High-Performance Asymmetric Supercapacitor Electrodes. *J. Mater. Chem.* **2012**, *22*, 153−160.
(43) Sumboja, A.; Foo, C. Y.; Wang, X.; Lee, P. S. Large Areal Mass, Flexible and Free-Standing Reduced Graphene Oxide/Manganese Dioxide Paper for Asymmetric Supercapacitor Device. *Adv. Mater.* **2013**, *25*, 2809−2815.
(44) Yu, Z.; Duong, B.; Abbitt, D.; Thomas, J. Highly Ordered MnO_2 Nanopillars for Enhanced Supercapacitor Performance. *Adv. Mater.* **2013**, *25*, 3302−3306.
(45) Hu, L.; Choi, J. W.; Yang, Y.; Jeong, S.; La Mantia, F.; Cui, L.-F.; Cui, Y. Highly Conductive Paper for Energy-Storage Devices. *Proc. Natl. Acad. Sci. U. S. A.* **2009**, *106*, 21490−21494.
(46) Kaempgen, M.; Chan, C. K.; Ma, J.; Cui, Y.; Gruner, G. Printable Thin Film Supercapacitors Using Single-Walled Carbon Nanotubes. *Nano Lett.* **2009**, *9*, 1872−1876.
(47) Xu, Y.; Lin, Z.; Huang, X.; Liu, Y.; Huang, Y.; Duan, X. Flexible Solid-State Supercapacitors Based on Three-Dimensional Graphene Hydrogel Films. *ACS Nano* **2013**, *7*, 4042−4049.
(48) Yang, X.; Cheng, C.; Wang, Y.; Qiu, L.; Li, D. Liquid-Mediated Dense Integration of Graphene Materials for Compact Capacitive Energy Storage. *Science* **2013**, *341*, 534−537.
(49) Lukatskaya, M. R.; Mashtalir, O.; Ren, C. E.; Dall'Agnese, Y.; Rozier, P.; Taberna, P. L.; Naguib, M.; Simon, P.; Barsoum, M. W.; Gogotsi, Y. Cation Intercalation and High Volumetric Capacitance of Two-Dimensional Titanium Carbide. *Science* **2013**, *341*, 1502−1505.

https://dx.doi.org/10.1021/acsnano.0c05903
ACS Nano XXXX, XXX, XXX−XXX